



BELLE Preprint 97-5

KEK Preprint 97-102

## Monte-Carlo Simulation for an Aerogel Čerenkov Counter\*

R. Suda<sup>a</sup>, M. Watanabe<sup>b</sup>, R. Enomoto<sup>c†</sup>, T. Iijima<sup>c</sup>, I. Adachi<sup>c</sup>, H. Hattori<sup>d</sup>, T. Kuniya<sup>e</sup>,  
T. Ooba<sup>b</sup>, T. Sumiyoshi<sup>c</sup>, and Y. Yoshida<sup>f</sup>

<sup>a</sup>*Tokyo Metropolitan University, Tokyo 192-03, Japan*

<sup>b</sup>*Chuo University, Tokyo 112, Japan*

<sup>c</sup>*High Energy Accelerator Research Organization, KEK, Ibaraki 305, Japan*

<sup>d</sup>*Chiba University, Chiba 260, Japan*

<sup>e</sup>*Saga University, Saga 840, Japan*

<sup>f</sup>*Toho University, Chiba 274, Japan*

---

\* Submitted to Nucl. Instrum. Meth. **A**.

†Electric Mail Address: enomoto@bsunsrv1.kek.jp.

## **Abstract**

We have developed a Monte-Carlo simulation code for an aerogel Čerenkov Counter which is operated under a strong magnetic field such as 1.5T. This code consists of two parts: photon transportation inside aerogel tiles, and one-dimensional amplification in a fine-mesh photomultiplier tube. It simulates the output photoelectron yields as accurately as 5% with only a single free parameter. This code is applied to simulations for a B-Factory particle-identification system.

PACS number : 29.40.Ka

keywords : aerogel, Fine-Mesh photo multiplier tube, Monte-Carlo

# 1 Introduction

Particle identification (PID), particularly the identification of charged pions and kaons, plays an important role in CP-violation studies in B-Factory experiments[1]. In the BELLE experiment at the KEK B-factory(KEKB), a threshold silica aerogel Čerenkov counter (ACC) will be used to extend the momentum region of the PID capability beyond the reach of  $dE/dx$  and time-of-flight (TOF) measurements[2].

Silica aerogels (aerogels) are a colloidal form of glass, in which globules of silica are connected in three-dimensional networks with siloxan bonds[3, 4]. Many high-energy and nuclear-physics experiments have used aerogels instead of pressurized gas for Čerenkov counters.

In the BELLE experiment, fine-mesh photomultiplier tubes (FM-PMTs) will be used for the readout of Čerenkov photons emitted from aerogel[5, 6]. This was only choice at the design period for this kind of counter operated under a strong magnetic field, such as 1.5T.

We have developed a Monte-Carlo simulation for the aerogel counter, which includes photon transportation in the aerogel tiles and response of a phototube. One of the key issue in this simulation is the parameterization of absorption length, which is obtained by a careful comparison of beam test data and the prediction from the simulation. We describe a Monte-Carlo simulation of this detector system in this paper. In the next section we introduce our experimental setup of the threshold Čerenkov counter. The purpose of this Monte-Carlo project is also described. The framework of this Monte-Carlo code is described in the third section. The simulation of fine-mesh phototubes is described in section 4, and photon transportation inside aerogel tiles is shown in section 5. In section 6, a simple model for aerogel absorption is introduced. The results on this model is described in section 7. In section 8, we discuss on the wavelength dependence of the light absorption. The conclusion is given in section 9.

## 2 Threshold Čerenkov Counter with a Fine-mesh Photomultiplier Tube Readout

We will use threshold Čerenkov counters to identify charged kaons in the momentum region 1-4 GeV. The configuration of the aerogel counter system of the BELLE detector is shown in Figure 1. It should be noted that the KEK B-factory is an asymmetric  $e^+e^-$  collider with energies of  $3.5 \times 8$  GeV and the produced particles from the B meson decay are Lorentz boosted to the  $e^-$ -beam direction(z). Since the momentum range of the produced pions and kaons changes as the emitted polar angle changes in a laboratory system, we employ the different refractive indices ( $n$ ) of aerogel tiles corresponding to the different polar angle. In the endcap region, however,  $n=1.03$  was selected for  $B$ -flavor tagging purpose[7].

The typical arrangement of the counter is shown in Figure 2. The size of an aerogel tile is approximately  $12 \times 12 \times 2.4$  cm<sup>3</sup>. The single counter contains 4, 5, or 6 layers of them with a total thickness of 10-14.5 cm. The Čerenkov photons are readout by one or two fine-mesh photomultiplier tubes (FM-PMT). In order to reduce effects of a magnetic field of 1.5T in the  $z$  direction, we selected the FM-PMT. We will use three types of FM-PMTs of 2, 2.5, and 3 inches in diameters. The effective diameters of these FM-PMTs are 39, 51, and 64 mm. The inner side of the counter is covered with a white reflector (Goretex[8]).

The dominant scattering mechanism of the Čerenkov photon inside the aerogel tile is considered to be Rayleigh scattering. There is almost no understanding about the absorption mechanism of the light inside aerogel. The main purpose of developing this Monte-Carlo code is to understand this mechanism, or in other words, to construct a reliable model.

The amplification mechanism of the FM-PMT in a strong magnetic field is also poorly

understood. Since the B-factory is a high-statistics experiment, an accurate Monte-Carlo simulation is necessary for these PMT's responses.

In summary, we would like to develop a Monte-Carlo simulation with an accuracy of a few percent level. It should simulate such effects as position dependence and edge effect.

### 3 Framework

The typical scattering length of aerogel is a few cm at  $\lambda = 400\text{nm}$  [4]. Therefore, Čerenkov photons undergo many scatterings (including absorptions and reflections) before reaching photocathodes. It is very difficult to understand this situation analytically. The Monte-Carlo simulation may be the only calculation choice.

In coding the Monte-Carlo simulation, we used C++ language. A part of GEANT3.21[9] was used for the geometry and display parts.

The flow chart of this Monte-Carlo simulation (hereafter, referred as “ACC++”) is shown in Figure 3. Each box corresponds to a major process in the program, which is written as “class” in C++. The vertical arrows indicate the direction of the data flow. The display and geometry parts are common utilities. At first the hit points by the charged particles inside the aerogels are recorded. Čerenkov photons are emitted at the above-mentioned hit points according to the velocity of the charged particles and the refractive index of medium. Then, the photon transport part takes care of photon transportation to the phototube window surface. Finally, the FM-PMT part amplifies the photoelectrons and the ADC counts are obtained. For data management, we used the CLHEP library[10].

### 4 Fine-mesh Photomultiplier-Tube Simulation

## 4.1 Structure of a Fine-mesh PMT

A sectional view of the FM-PMT is shown in Figure 4. Each PMT has a borosilicate glass window, a bialkali photocathode, 19 fine-mesh dynodes and an anode. The diameters of the effective area( $\phi$ ), equal to the diameters of the dynodes, are 39, 51, and 64mm for 2", 2.5", and 3" PMTs, respectively. The cathode-to-anode distances(L) are 20, 20, and 23mm for 2", 2.5", and 3" PMTs, respectively. The FM-PMT used for the BELLE ACC has the following improved performance. The average quantum efficiency(QE) of the photocathode is 25% at 400nm wavelength, improved for recent products [11]. A finer mesh than that of conventional products is used to improve the gains in the magnetic fields [6]. The optical opening of the mesh is about 50%[12].

## 4.2 Simple Model of Amplification

The first step of the simulation is conversion of incident photons to photoelectrons(p.e.). This conversion is simulated while taking into account the wavelength dependence of the quantum efficiency(QE). Numerical data of the wavelength dependence, obtained from the manufacturer, are used. The absolute value of QE for each PMT is determined by the cathode blue sensitivity, denoted as  $Skb$ [11]. The absolute QE at 400nm wavelength(QE(400nm)) can be calculated as

$$QE(400nm) = 0.026 \times Skb \quad (1)$$

using the data obtained from the manufacturer. The QE does not depend on the diameter of the PMT. The average  $Skb$  value is 9.7.

The second step is to simulate the amplification in fine-mesh dynodes. A simple model is schematically shown in Figure 5. For each dynode stage, some incident electrons pass through holes of a fine-mesh dynode, and others hit the dynode wires, followed by the emission of secondary electrons. The probability of passing through holes is proportional

to the optical opening(the ratio of the hole area to the total area) of the mesh,  $f$ ( $\sim 0.5$ ). Some of the secondary electrons pass through the holes, and others are re-absorbed by the same wire. The re-absorption probability is dependent on the hit position, and it is higher when electrons hit the mesh at the top of wires, compared to the case when they hit it at the edge. That probability increases at higher magnetic fields. This dependence is considered in the simulation by introducing a blind region, where all of the secondary electrons are assumed to be re-absorbed. The ratio of the blind region area to the total dynode area is represented by a parameter  $b$  in the simulation. The effective gain per one stage of a dynode( $\delta^{eff}$ ) is then parameterized as

$$\delta^{eff} = f + \delta^{hit}(1 - f - b), \quad (2)$$

where  $\delta^{hit}$  is the number of secondary electrons passing through holes, whose distribution is assumed to be a Poisson in the simulation. The quantity  $\delta^{hit}$  is determined so that the total gain for the 19 stages( $G$ ) is reproduced. Since the gains of the first three and the last two dynodes of our FM-PMTs are improved by a factor of  $k$ [12], we obtain

$$k^5 \times (\delta^{eff})^{19} = G. \quad (3)$$

Here,  $\delta^{eff}$  is typically around 2.5[12].

In a simulation of the pulse height for each incident photoelectron, the above process is repeated until the sixth dynode. It is shown later that a calculation up to the sixth dynode is sufficient to reproduce the pulse-height spectrum.

### 4.3 Single-photoelectron Spectrum

Using the method described in section 4.2, a pulse-height spectrum for single-photoelectron events is simulated, as shown in Figure 6-(a). That is compared to the experimental data shown in Figure 6-(b). The experimental data were taken by using a pulsed laser[13]. The

number of events in the pedestal region is more than 90% of the total events. Therefore, most of the signal events are single-photoelectron events.

The simulation reproduces the experimental data well. The single-photoelectron spectrum of FM-PMTs has no characteristic peak, in contrast with that of line-focus PMTs. Only a fractal structure is observed in the spectrum, the interpretation of which is described in reference [5].

#### 4.4 Multi-photoelectron spectrum

As noted in section 4.3, a FM-PMT has no peak corresponding to a single photoelectron in the spectrum. This deteriorates the pulse-height resolution of a multi-photoelectron spectrum, compared to the resolution determined by the original Poisson distribution of incident photoelectrons.

Figure 7 shows a comparison of the incident photoelectron distribution(a) and the simulated spectrum at the anode for corresponding events(b). To quantitate the deterioration, we define the excess noise factor( $ENF$ ) as

$$ENF = \frac{\mu_{input}}{\mu_{eff}}, \quad (4)$$

where  $\mu_{input}$  is the average number of input photoelectrons and  $\mu_{eff}$  is the effective number of output photoelectrons. In the present work, the output spectrum is fit to an asymmetric Gaussian with two width parameters ( $\sigma_1$  and  $\sigma_2$ ), each representing the width of the lower and higher sides, respectively, as shown in Figure 7-(b). Then  $\mu_{eff}$  is calculated as

$$\mu_{eff} = \left( \frac{\bar{n}}{\sigma_1} \right)^2, \quad (5)$$

where  $\bar{n}$  is the mean of the spectrum (mean ADC count). In the example shown in Figure 7,  $\mu_{input}$  is 20.0 and  $\mu_{eff}$  is 9.64. Therefore,  $ENF$  is 2.07.



Figure 8 shows the measured  $ENF$  for 2", 2.5", and 3" PMTs. The tested PMTs were illuminated by the same 412nm pulsed laser light. The number of incident photons was calibrated using a reference PMT, that is a 2" line-focus type PMT (Hamamatsu R329-05S), which was well calibrated by the manufacturer. The average number of photoelectrons( $\mu_{input}^{data}$ ) was deduced from the average ADC channel( $\bar{q}$ ) and gain. The gain was obtained from the mean ADC channel for a single-photoelectron event( $q_0$ ). Taking into account of the difference in the quantum efficiency between the reference PMT( $QE(\text{ref})$ ) and the tested FM-PMT( $QE(\text{FM})$ ), the number  $\mu_{input}^{data}$  was obtained as

$$\mu_{input}^{data} = \frac{QE(\text{FM})}{QE(\text{ref})} \frac{\bar{q}}{q_0}. \quad (6)$$

The quantum efficiencies ( $QE(\text{FM})$  and  $QE(\text{ref})$ ), measured by the manufacturer have about a 10% ambiguity, giving about a 14% error in the measured  $ENF$ [12]. The measured  $ENF$  is 1.99 on the average. The agreement between the simulation and the data is satisfactory.

## 4.5 Effect of a Magnetic Field on the Resolution

The electron trajectories are influenced by magnetic fields. In the simulation, the effects of magnetic fields are treated as follows.

On the microscopic scale, electrons spiral along the magnetic field. At 1.5T, the Lamor radius of electrons for a typical energy of 6eV is  $5.5\mu\text{m}$ , which is comparable to the mesh width. Therefore, the probability for the re-absorption of secondary electrons by mesh wires increases. This effect can be regarded as an increase in the blind region( $b$ ) on the mesh, which is shown in Figure 5, not only as a decrease in  $\delta^{hit}$ . The increase in  $b$  affects the pulse-height resolution, while a decrease in  $\delta^{hit}$  affects the total gain.

On the macroscopic scale, electrons move parallel to the direction of the magnetic field. Therefore, some electrons can not reach the anode when the PMT axis is inclined

with respect to the magnetic field. The fraction of such electrons is determined by the diameter of the photocathode( $\phi$ ) and the cathode-to-anode distance(L). In the simulation, the position of secondary electrons on the anode plane is calculated from information about the positions of electrons at the cathode and the field direction. Then, in case that an electron is in the effective area of the anode, the amplification process is simulated.

Table 1 shows the ratio of the effective number of photoelectrons with magnetic fields of 1.5Tesla ( $\mu_{eff}(1.5T)$ ) to that without magnetic fields ( $\mu_{eff}(0T)$ ), obtained from our simulation and a measurement for each PMT size. The results are shown for  $\theta = 0^\circ$  and  $35^\circ$ , where  $\theta$  is the angle between the PMT axis and the fields. The parameter  $b$  is adjusted to reproduce the experimental data for each angle. In the case of  $\theta = 0^\circ$ , the experimental data can be reproduced well with  $b = 0.15$ . In the case of  $\theta = 35^\circ$ , the results of the simulation are shown for two cases,  $b = 0$  and  $b = 0.15$ . A better agreement between the data and the simulation is obtained when only the macroscopic effect is considered ( $b = 0$ ). Therefore, it is indicated that the macroscopic effect dominates for  $\theta = 35^\circ$  case. The dependence of the parameter  $b$  on the angle  $\theta$  can be explained by a change of the mesh width projected along the magnetic field direction.

## 5 Photon Transport inside Aerogel Tiles

### 5.1 Algorithm

A charged particle is transported inside aerogels by a 1-mm step. Čerenkov photons are radiated along the charged-particle's trajectory. The number of photons ( $N_p$ ) is given by the Frank-Tamm equation [14],

$$\frac{dN_p}{dE} = \left(\frac{\alpha}{\hbar c}\right) L z^2 \sin^2 \theta_c, \quad (7)$$

where  $\alpha$  is the fine-structure constant,  $L$  the thickness of the radiator,  $z$  the charge of an incident particle,  $\theta_c$  the Čerenkov angle, and  $E$  the energy of a radiated photon. The Čerenkov angle ( $\theta_c$ ) for a particle with velocity  $\beta c$  in a medium with index of refraction ( $n$ ) is

$$\theta_c = \cos^{-1}\left(\frac{1}{\beta n}\right). \quad (8)$$

A radiated photon is transported according to the algorithm shown in Figure 9. In the photon-transport part, we first obtain information about photon, i.e., the wavelength, radiated position, and radiated direction from the Čerenkov-radiation part.

The Čerenkov photon is transported to the next position in the following way. The mean transport length ( $\Lambda$ ) is defined as

$$\frac{1}{\Lambda(\lambda)} = \frac{1}{\Lambda_{scat}(\lambda)} + \frac{1}{\Lambda_{abs}(\lambda)}, \quad (9)$$

where  $\Lambda_{scat}$  and  $\Lambda_{abs}$  are the scattering length, and absorption length respectively, in the aerogel. They are calculated based on the spectrophotometer measurement, which is described in section 5.2.1. The transport length is calculated using the exponential probability function (Poisson distribution). It is then judged that the position after transport is (i) outside the counter box or (ii) inside with the information from the Geometry part, in which we used GEANT 3.21 (only geometry routines)[9]. (i) If the position is out of the box, the photon is traced to the inner wall of the box. We then judge whether the position is on the FM-PMT surface or diffuse reflector surface (Goretex [8]). If the position is on the FM-PMT surface, the photon information (the wavelength and the position of hit) is given to FM-PMT simulation part and the photon transport is finished. If the photon hits a reflector surface, we judge whether the photon is absorbed or reflected by Goretex based on a spectrophotometer measurement of the Goretex reflectivity, which is described in section 5.2.2. If the photon is absorbed by Goretex, the photon transport is finished. If the photon is reflected by Goretex (diffuse reflection), the photon is transported again.

(ii) If the position after transportation is in the counter box, it is judged that the photon is absorbed or scattered by aerogel, according to the following ratios:

$$P_{abs} = \frac{\Lambda_{scat}}{\Lambda_{scat} + \Lambda_{abs}}, \quad (10)$$

$$P_{scat} = \frac{\Lambda_{abs}}{\Lambda_{scat} + \Lambda_{abs}}, \quad (11)$$

where the  $P_{abs}$  and  $P_{scat}$  are the probability of absorption and the scattering of the aerogel, respectively. If the photon is absorbed by aerogel, the photon transport is finished. If the photon is scattered by aerogel, we randomize the direction according to the Rayleigh-scattering formula and repeat the above-mentioned transportation again.

## 5.2 Input Parameters

### 5.2.1 Spectrophotometer Measurement

We use the spectrophotometer[15] in order to measure the transmittance of aerogel and reflectivity of Goretex as a function of the wavelength(250 ~ 800 nm). The transmittance ( $T$ ) is defined as  $I/I_0$ , where  $I$  and  $I_0$  are the photon fluxes at the photodetector with and without aerogels, respectively. The thickness of a typical aerogel tile is 24mm. The spectrophotometer has a finite solid angle at the entrance of the photo detector. A part of scattered photons is detected by the photodetector. Therefore, the transmittance ( $T$ ) is

$$T \neq 1 - A, \quad (12)$$

$$T \neq 1 - A - S, \quad (13)$$

where  $A$  is the absorption and  $S$  is the scattering. In order to estimate the contribution from  $S$  and  $A$  to  $T$ , we took the geometry of the photospectrometer and other necessary information into account for our Monte-Carlo (ACC++) and carried out a simulation.

The details are discussed in section 5.2.3. A simulation display of the photospectrometer is shown in Figure 10. The lines are the photon trajectories. The circle is the aperture of the photodetector ( $8\text{mm}\phi$ ).

### 5.2.2 Goretex Reflectivity

It is not possible to measure the absolute reflectivity of a material directly with the spectrophotometer. We therefore measure the relative reflectivities of samples to a reference sample whose absolute reflectivity is known. We used an NIST traceable standard reflector (Spectralon) which was well calibrated by a company[16]. Then, the absolute reflectivity of Goretex was calculated. Figure 11 shows the measured absolute reflectivity of the Goretex as a function of the wavelength. The reflectivity of Goretex is better than 93% over the range of the measurement. It shows a better reflectivity in the short-wavelength region, i.e., a better acceptance for Čerenkov light (UV light).

### 5.2.3 Rayleigh Scattering

We input two parameters ( $\Lambda_{abs}$  and  $\Lambda_{scat}$ ) in the simulator. Initially, we suppose that the transmittance is only due to the Rayleigh-scattering effect. We consider the absorption and scattering parameter, as expressed below by Equations 14 and 15, and input them to the simulator:

$$\Lambda_{abs} = \infty, \tag{14}$$

$$\Lambda_{scat} = \frac{-d}{\ln T}, \tag{15}$$

where  $d$  is the thickness of the samples. Although the simulated transmittance shows almost the same shape as the experimental transmittance, the absolute value of the simulated data points are higher than the experimental data (i.e., more transparent). This indicates that the scattered events within the finite solid angle of the photodetector and

the absorption events are taken into account for the transmittance. We must take these factors into account. Then, the aperture factor ( $f_a$ ) is introduced in Equation 16 and the definition of  $\Lambda_{scat}$  is modified to

$$\Lambda_{scat} = f_a \times \frac{-d}{\ln T}. \quad (16)$$

To evaluate the aperture factor ( $f_a$ ), a simulation was carried out. The obtained value for  $f_a$  is 0.55. Figure 12 shows the transmittance data and simulation result, which agree with each other. In other words, the photospectrometer measurement of our aerogels suggests that there is no, or very small, absorption.

## 6 Model for Absorption

Empirically, it was known that the transmittance obtained by the spectrophotometer was well fitted with the two terms:

$$\Lambda_{scat} = a\lambda^4, \text{ and } \Lambda_{abs} = b\lambda^2, \quad (17)$$

where  $\lambda$  is the wavelength and  $a$  and  $b$  are free parameters. The  $\lambda^2$  term was empirically introduced in order to improve the fitting of the transmittance spectra. In the reference[17], they assumed that the  $\lambda^4$  term is the Rayleigh scattering, and that the  $\lambda^2$  term is the absorption. The results ( $n=1.010$ ) are shown in Figure 13 for our aerogel.

The typical scattering length was calculated to be  $\sim 2.5$  cm at 400 nm wavelength, and the absorption length was fitted to be 10-times the scattering length. When we input parameters  $\Lambda_{scat}$  and  $\Lambda_{abs}$  into our Monte-Carlo simulation (ACC++), we obtained only  $\sim 2$  photo-electrons (p.e). On the other hand, an experiment using 3.5 GeV  $\pi^-$  beam was carried out for our counter box (Figure 2); we obtained  $\sim 20$  p.e., which is inconsistent with the above assumption. Therefore, we conclude that  $b\lambda^2$  is not due to absorption, and that the absorption length is greater than 100-times the scattering length.

In order to estimate the magnitude of the absorption length, we make a simple model that the absorption length is proportional to the scattering length, i.e., we assume the same wavelength dependence as that of the Rayleigh scattering,

$$\Lambda_{abs} = \alpha \times \Lambda_{scat}, \quad (18)$$

where  $\alpha$  is a free parameter. The  $\alpha$  value was determined by comparing the experimental data and simulation results as described in the next section. We then input these two parameters ( $\Lambda_{abs}$  and  $\Lambda_{scat}$ ) into ACC++. Figure 14 shows a simulation display of ACC++ for the photon transportation inside the aerogel tile with the assumption  $\alpha=100$ . The other type of absorption model can be found, for example, in reference[18].

## 7 Comparison between the Beam-Test Results and Simulation

### 7.1 Determination of $\alpha$ by $\chi^2$ Minimization

We carried out a  $\chi^2$  minimization by comparing the  $\mu_{eff}$  value of the experimental data and that of the Monte-Carlo data while changing the free parameter ( $\alpha$ ). The experimental data were obtained in the beam test with the 3.5-GeV  $\pi^-$  at the  $\pi 2$  beam line of the KEK PS. The incident position of the  $\pi^-$ 's is the center of the box. Figure 15 shows this result. From the minimum of this curve we obtained  $\alpha = 408.1 \pm_{58.5}^{68.3}$  which corresponds to an absorption length ( $\Lambda_{abs}$ ) of about 5.4 m at 400 nm. The  $\alpha$  values differ (by a factor of  $\sim 2$ ) for different samples of aerogels having the same refractive index and a different refractive index. There are no clear dependence on transmittance nor refractive indices. We, therefore, must obtain this value for each counter box, for example using  $e^+e^- \rightarrow \mu^+\mu^-$  events in the real B-factory experiment.

## 7.2 Position Dependence and Accuracy

With the best-fitted  $\alpha$  value we compared the beam data and the Monte-Carlo prediction for the position dependence of light yields. The experimental data of  $\mu_{eff}$  were obtained for the 3.5-GeV  $\pi^-$ . The data were taken at various positions of the incident beam. We selected 23 incident positions. The coordinate system of the beam incident position and direction are defined in Figure 16. The beam direction is  $(0, 0, 1)$  for all data. A comparison with the Monte-Carlo data are shown in Figures 17: (a) at  $y=0$  plane, (b)  $y=2\text{cm}$ , (c)  $y=3.5\text{cm}$ , and (d)  $y=4\text{cm}$ . The hatched areas are the Monte-Carlo predictions. These errors are statistical. The disagreements between the experiment and Monte-Carlo values are around the 5% level. We therefore consider the accuracy of our Monte-carlo simulation to be 5%.

## 7.3 Miscellaneous Distributions

With the best-fitted value of the parameter  $\alpha$ , we derived the distributions of the number of scatterings inside the aerogel which our Monte-Carlo simulation predicts. They are shown in Figure 18. The mean number of reflections on the Goretex is  $\sim 11$ -times, that of the scattering in aerogel is  $\sim 29$ -times, and mean total transport length is  $\sim 83$  cm. 43% of initial radiated photons in aerogel reach the PMT surface, 32% are absorbed by Goretex, and 25% are absorbed by aerogel. This Monte-Carlo code is very useful in designing the shape of the counter box for future experiments.

# 8 Wavelength Dependence of Absorption

As noted in section 7.2, our Monte-Carlo simulator is able to reconstruct beam data with 5% accuracy after fitting the  $\alpha$  value. For a further study to evaluate the wavelength dependence of the absorption length( $\Lambda_{abs}$ ), we carried out experiments with several types of



optical filters (sharp-cut filters [19]). These filters cut the light with a shorter wavelength than threshold values. Here, we define the filter's name, whose threshold wavelength is 300nm, 300nm-filter. We used eight types of filters, whose threshold wavelengths are 300nm, 360nm, 400nm, 460nm, 500nm, 560nm, 600nm, and 700nm. The transmittance of each filter was measured with spectrophotometer as a function of the wavelength and input to ACC++.

The beam-test setup and evaluation procedure of the  $\alpha$  value were the same as those mentioned in section 7.1. The refractive index of aerogel was  $n = 1.013$ . We used a 3" FM-PMT with a 2" mask, because the diameter of the filters were 2". The filter was set between the PMT surface and the aerogel tiles. After fitting beam data with the simulation results, we obtained the best  $\alpha$  value for each filter setup,  $\alpha = 302.7 \pm 6.8^{7.0}$  for the 300nm filter,  $\alpha = 596.8 \pm 30.8^{32.5}$  for the 360nm filter,  $\alpha = 3104.5 \pm 611.5^{761.4}$  for the 400nm filter and  $\alpha$  diverges for the longer-wavelength filters. These are plotted in Figure 19 as a function of the threshold wavelength of the filter. From these  $\alpha$  values, we can conclude that  $\Lambda_{abs}$  is not proportional to  $\lambda^4$ . The absorption is significant only in short-wavelength range (around 300nm), but not in the longer wavelength region ( $>400$ nm).

Another absorption model, which assumes  $\Lambda_{abs} = \exp(\beta\lambda)$ , is found in the reference [18]. Here  $\beta$  is a free parameter. An attempt to evaluate  $\beta$  was carried out using the  $\chi^2$  minimization with the center incidence data. Then we looked at the wavelength dependence (experimental data with the sharp-cut filters) of the  $N_{pe}$ . In the result, we find that  $\beta$  is still dependent on the threshold wavelength of filter. The  $\beta$  value increases at longer wavelength. This again suggests that the absorption only happens at short wavelength such as 300nm.

## 9 Conclusion

We have developed a Monte-Carlo Simulation for an aerogel Čerenkov counter under a strong magnetic field. This code consists of two parts: photoelectron amplification in a fine-mesh phototube, and photon transportation inside aerogel tiles.

In the former, we have developed a simple one-dimensional fractal-amplification model. It successfully reproduces the deterioration of the resolution and the single-photoelectron response in a fine-mesh phototube.

In the latter, we have proven that recently produced aerogels have a significantly longer absorption length, such as longer than a few meters. Here, a simple model agrees with the experimental observations. This model only uses a single free parameter.

With this Monte-Carlo simulation code, we can simulate effective photoelectron yields within 5% ambiguities for various shape of counters, whose geometry can be defined in the GEANT framework. This program will be used for a particle-identification system for the KEK B-Factory, BELLE experiment.

## Acknowledgment

We would like to thank the BELLE collaboration of the KEK B-Factory for its help in this project. We would especially like to thank Prof. N. Katayama (KEK) for coding this program in C++ language. We also appreciate the authors of GEANT 3.21 and CLHEP. We are grateful to Prof. T. Hirose (Tokyo Metropolitan Univ.), Prof. S. Matsumoto (Chuo Univ.), and Prof. A. Murakami (Saga Univ.) for valuable comments on this manuscript.

The aerogels were developed under collaborative research between Matsushita Electric Works Ltd. and KEK. We would finally like to thank Hamamatsu Photonics K.K. for developing the fine-mesh photomultiplier tubes.

## References

- [1] T.Iijima et al., Nucl. Instrum. Meth. **A379** (1996) 457.
- [2] Belle collaboration, “Technical Design Report”, KEK Proceedings 95-1.
- [3] I.Adachi *et al.*, Nucl. Instrum. Meth. **A355** (1995) 390.
- [4] S.K.Sahu et al., Nucl. Instrum. Meth **A382** (1996) 441.
- [5] R.Enomoto et al., Nucl. Instrum. Meth. **A332** (1993) 129.
- [6] T.Iijima et al., Nucl. Instrum. Meth. **A387** (1997) 64.
- [7] R.Aleksan, J.Bartlet, P.R.Burchat, and A.Seiden, Phys. Rev. **D39** (1989) 1283.
- [8] Japan Goretex Co Ltd. Spec. No. 116-027.
- [9] R. Brun, M. Hansroul, and J. C. Lassalle, GEANT User’s Guide, CERN DD/EE/82.
- [10] L. Lönvlad, Comp. Phys. Comm. **84** (1994) 307.
- [11] See PMT catalogue of Hamamatsu Photonics K.K., TPMH 1110E01, Oct., 1995.
- [12] Private communication with T. Hakamata, Hamamatsu Photonics K. K.
- [13] Hamamatsu. Pico-sec Light Pulser PLP-02.
- [14] Frank and Tamm, C. R. Ac. Sci. U.S.S.R. **14** (1937) 109.
- [15] Hitachi Co Ltd. model U-3210.
- [16] Spectralon diffuse reflectance standards, Labsphere.
- [17] Proc. on “Workshop on physics and detector issues for a high-luminosity asymmetric B factory at SLAC”, SLAC-373, p484.

[18] K. Arisaka et al., Nucl. Instrum. Meth. **A385** (1997) 74.

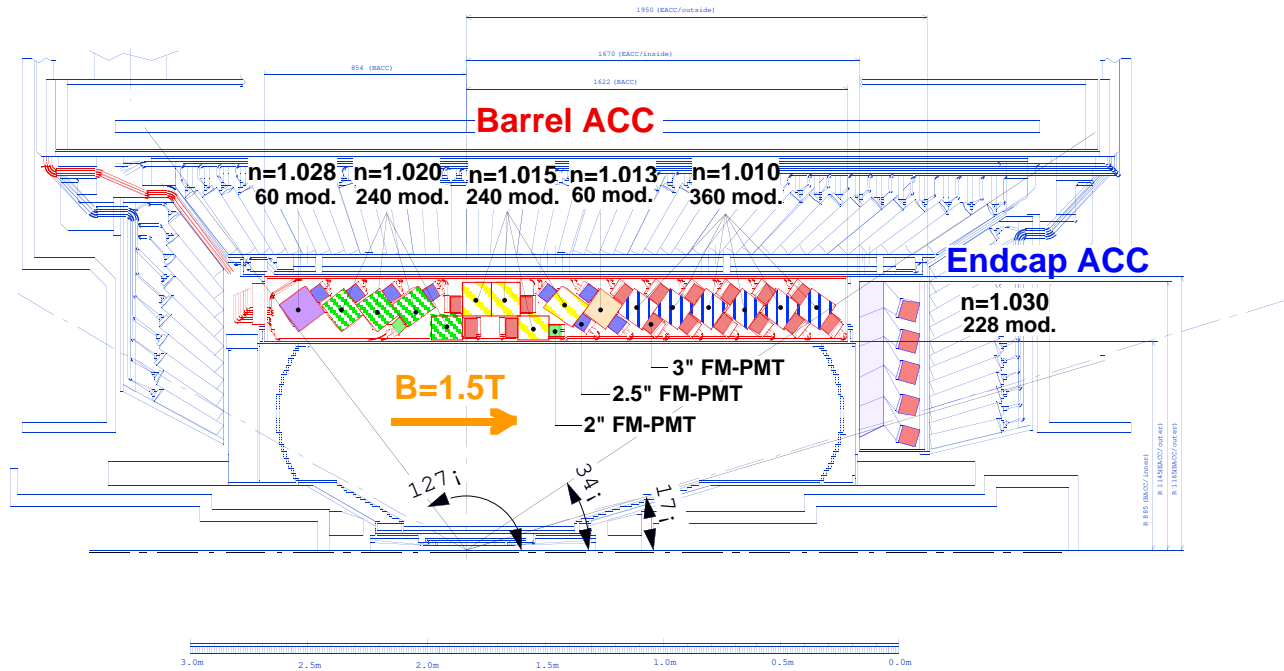
[19] Sharp-cut filter, SIGMA KOKI K.K. Japan.

## Table 1, R.Suda et al., NIM-A

Table 1: Ratio of the effective number of photoelectrons with magnetic fields of 1.5 Tesla ( $\mu_{eff}(1.5T)$ ) to that without magnetic fields ( $\mu_{eff}(0T)$ ) for 2", 2.5", and 3" PMTs for our simulation(MC) and experimental data(Data). The detail on  $\mu_{eff}$  can be found in the text.

		2"	2.5"	3"
$\theta = 0^\circ$	MC	0.72	0.70	0.70
	Data	0.76	0.75	0.74
$\theta = 35^\circ$	MC	0.62	0.65	0.64
		0.47	0.39	0.34
	Data	(b=0) 0.59	(b=0) 0.69	(b=0) 0.67
		(b=0.15)	(b=0.15)	(b=0.15)

Figure 1, R.Suda et al., NIM-A



inner-960729-half

Figure 1: BELLE aerogel Čerenkov-counter system (ACC) and BELLE detector.

Figure 2, R.Suda et al., NIM-A

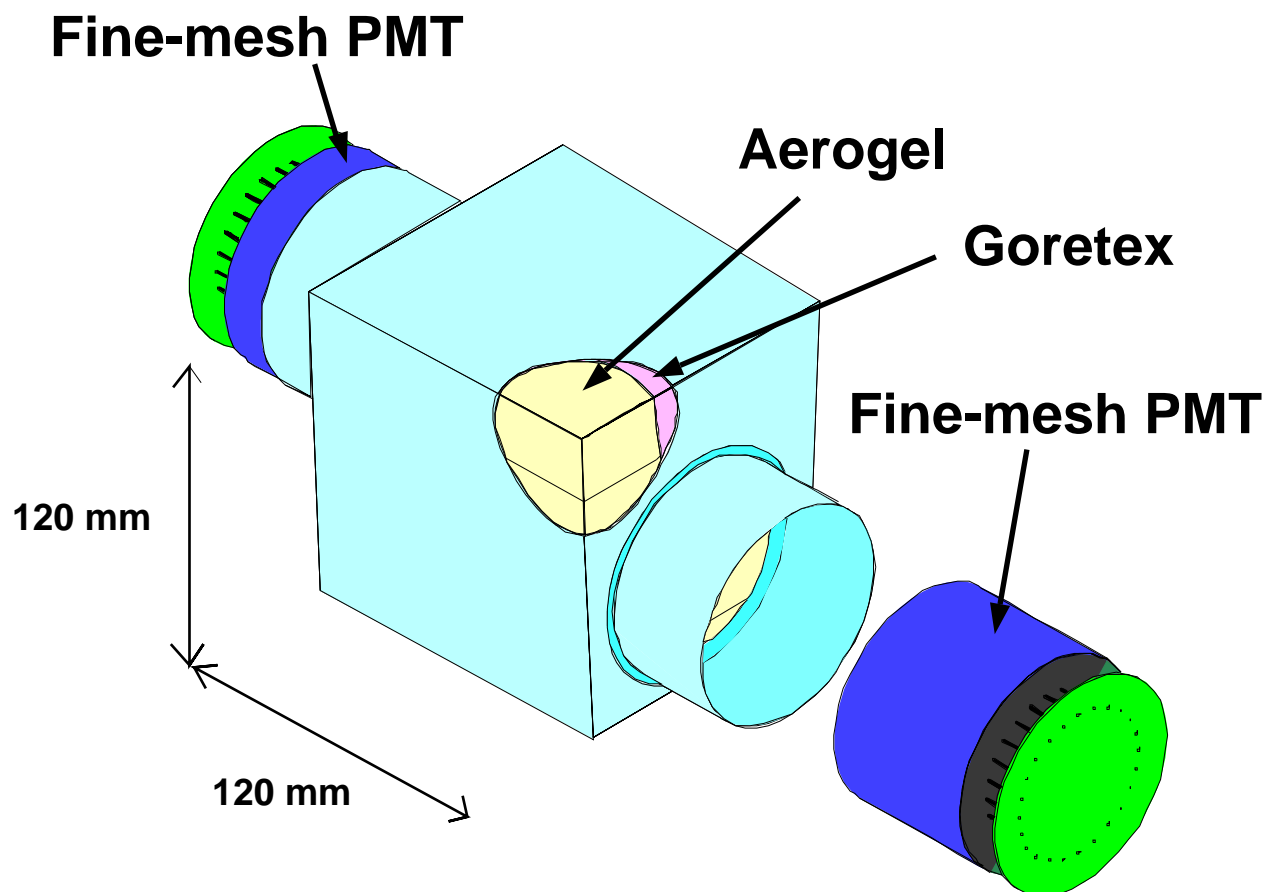


Figure 2: Typical form of the aerogel Čerenkov counter.

Figure 3, R.Suda et al., NIM-A

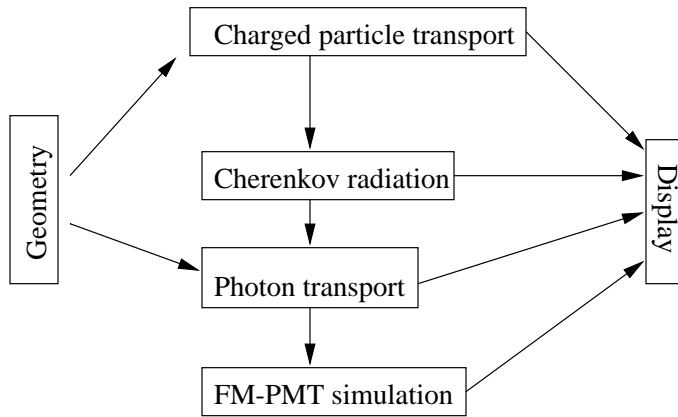


Figure 3: Flow chart of the Monte-Carlo simulation code (ACC++).



Figure 4, R.Suda et al., NIM-A

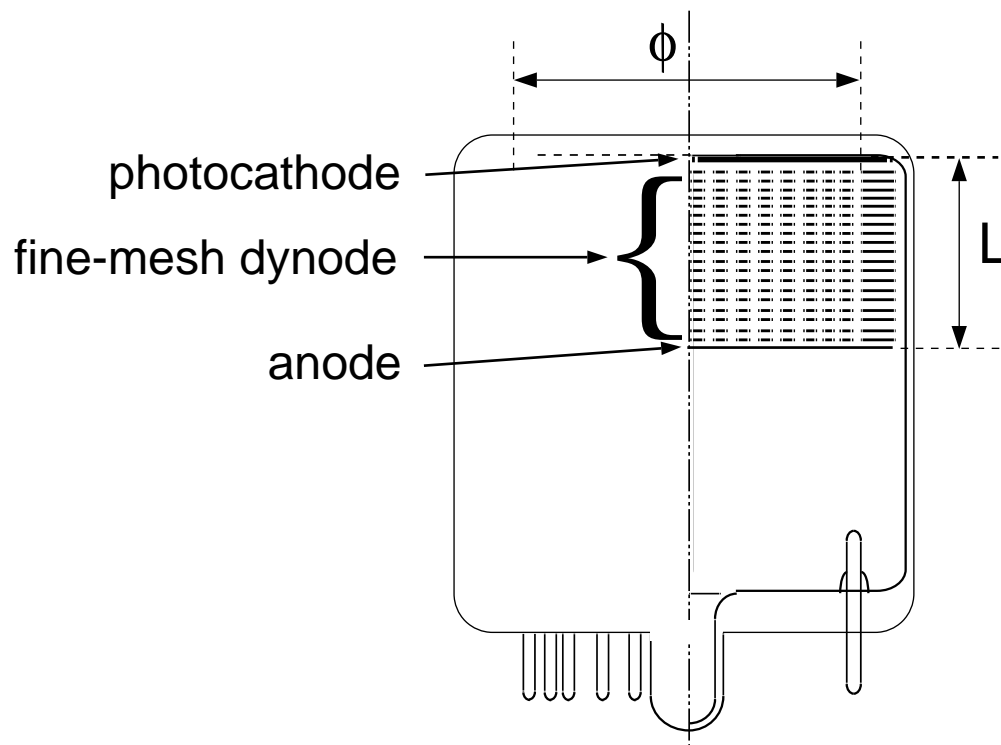


Figure 4: Sectional view of FM-PMT.

Figure 5, R.Suda et al., NIM-A

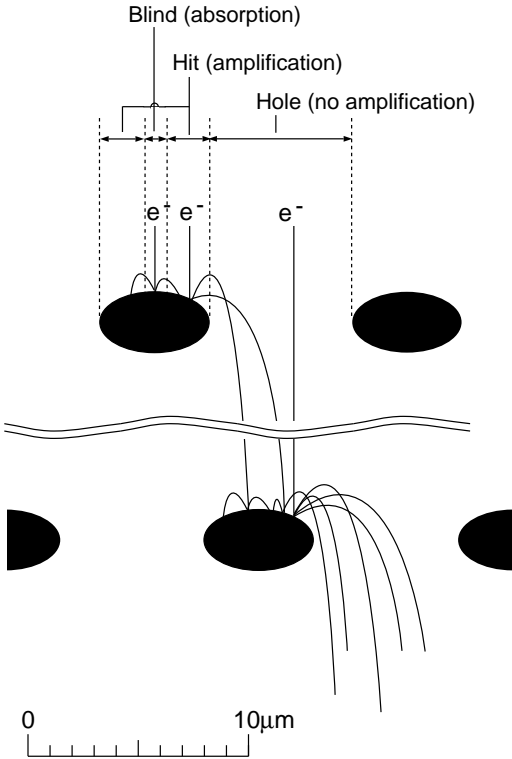


Figure 5: Model of the amplification by fine-mesh dynodes.

Figure 6, R.Suda et al., NIM-A

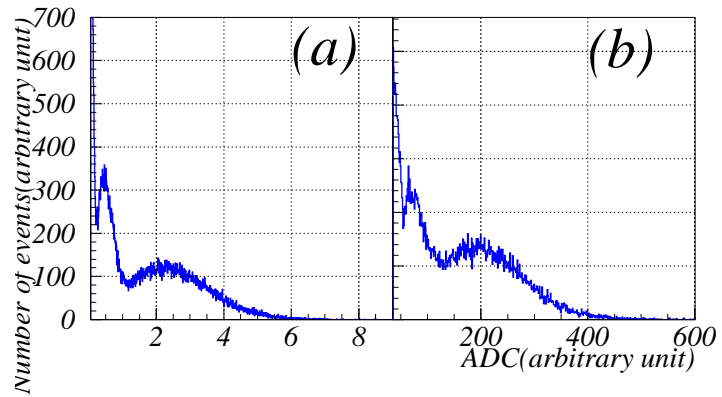


Figure 6: Single photoelectron spectra: (a) simulated spectrum and (b) experimental data.

Figure 7, R.Suda et al., NIM-A

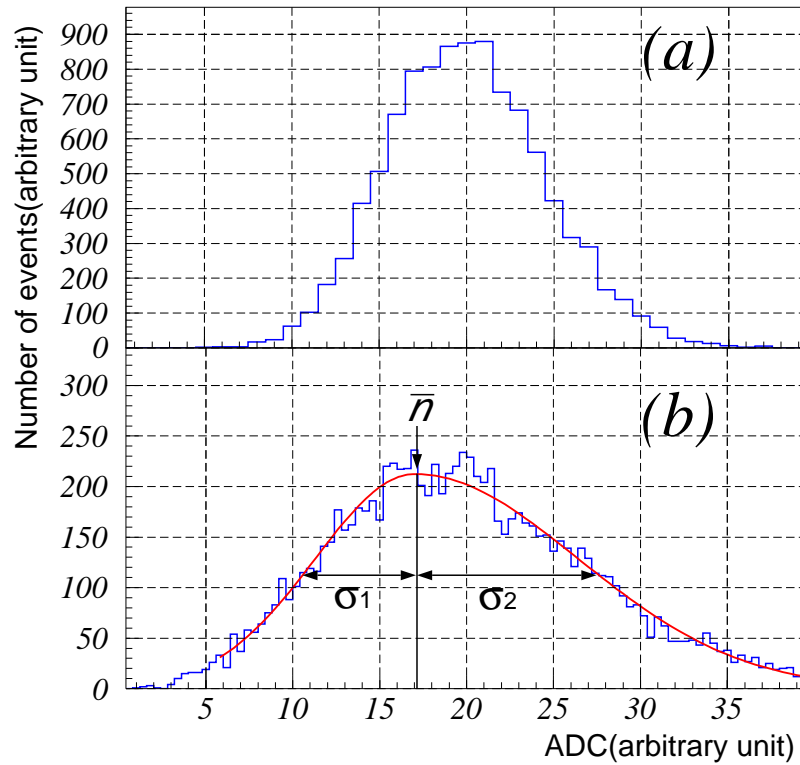


Figure 7: Simulated multi-photoelectron spectra: (a) the spectrum of incident photoelectrons and (b) output photoelectrons.

Figure 8, R.Suda et al., NIM-A

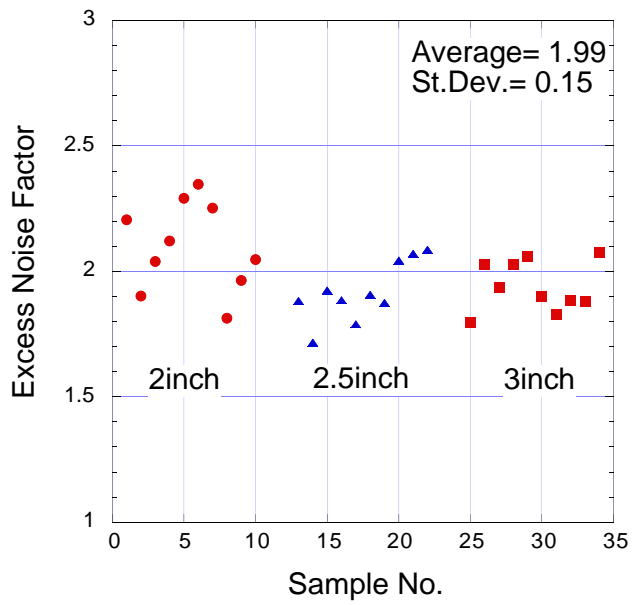


Figure 8: Measured Excess Noise Factor ( $ENF$ ) for 2", 2.5", and 3" PMT.

Figure 9, R.Suda et al., NIM-A

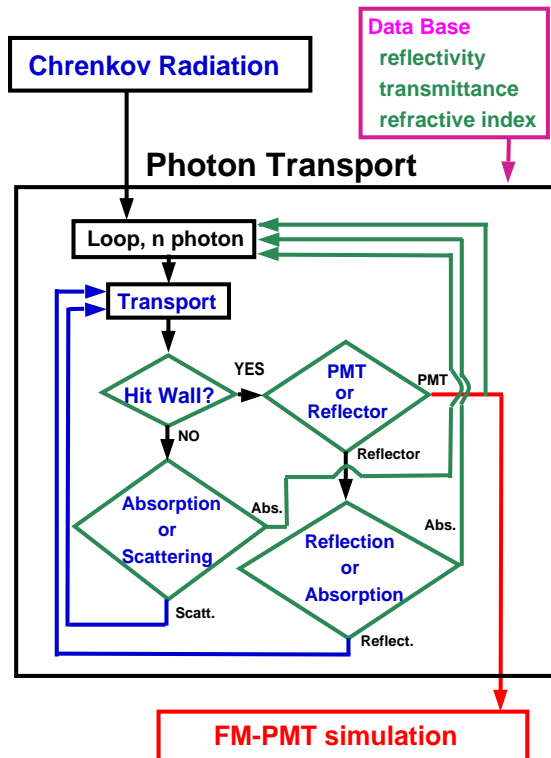


Figure 9: Algorithm of the photon transport part of the Monte-Carlo (ACC++).

**Figure 10, R.Suda et al., NIM-A**

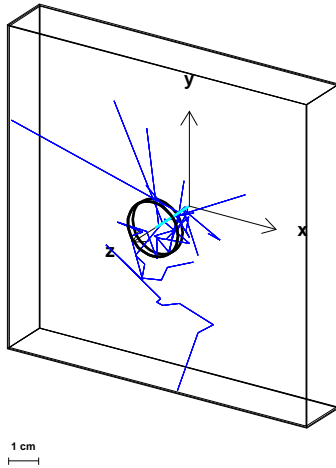


Figure 10: Event display of the spectrophotometer simulation. The lines are the photon trajectories. The circle is the aperture of the photodetector.

Figure 11, R.Suda et al., NIM-A

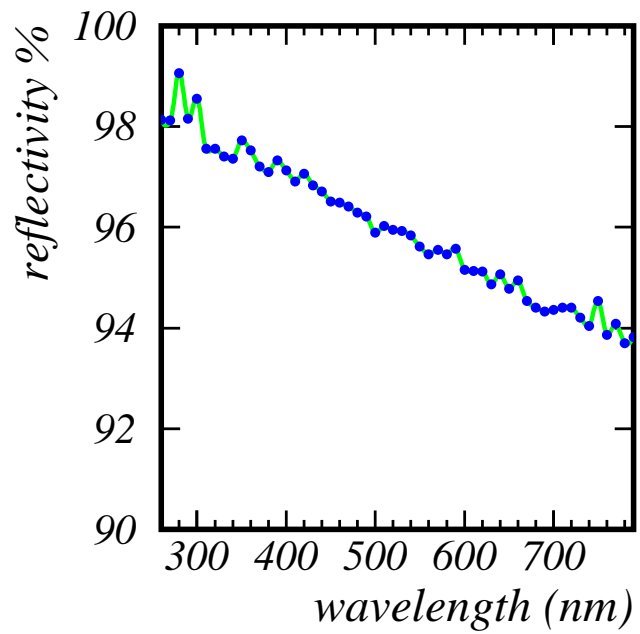


Figure 11: Reflectivity of the Goretex as a function of the wavelength obtained by the spectrophotometer.



Figure 12, R.Suda et al., NIM-A

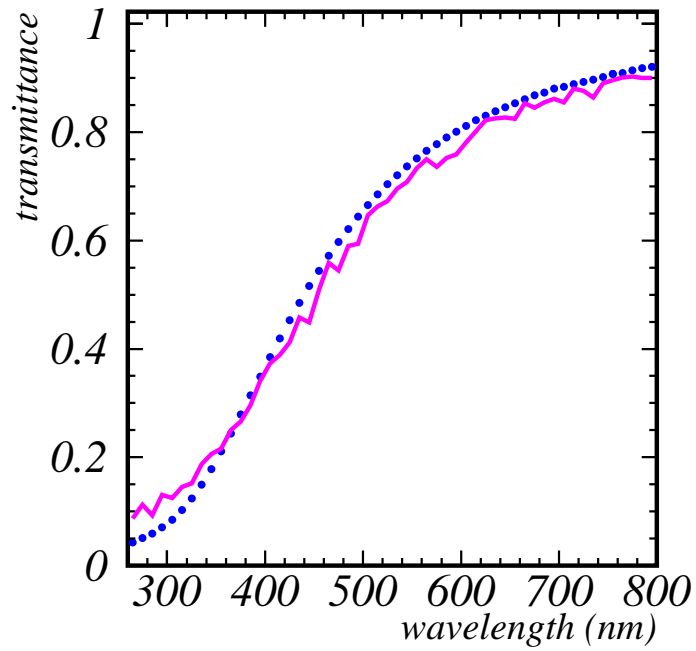


Figure 12: Data for the transmittance of  $n = 1.010$  aerogel (2.4cm thick). The solid line is the simulation result with only Rayleigh scattering.

Figure 13, R.Suda et al., NIM-A

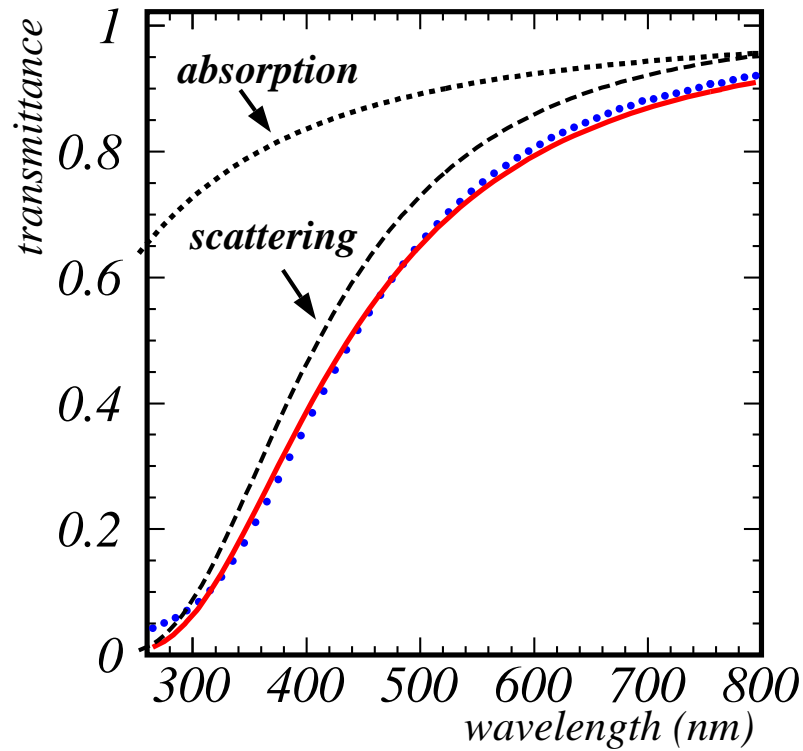


Figure 13: Transmittance(circles) measured by the spectrophotometer for  $n=1.010$ , 2cm-thick aerogel; the solid curve is the best fit with the parameterization (Equation 17), the dotted line contribution of absorption, and the dashed line that of scattering.

Figure 14, R.Suda et al., NIM-A

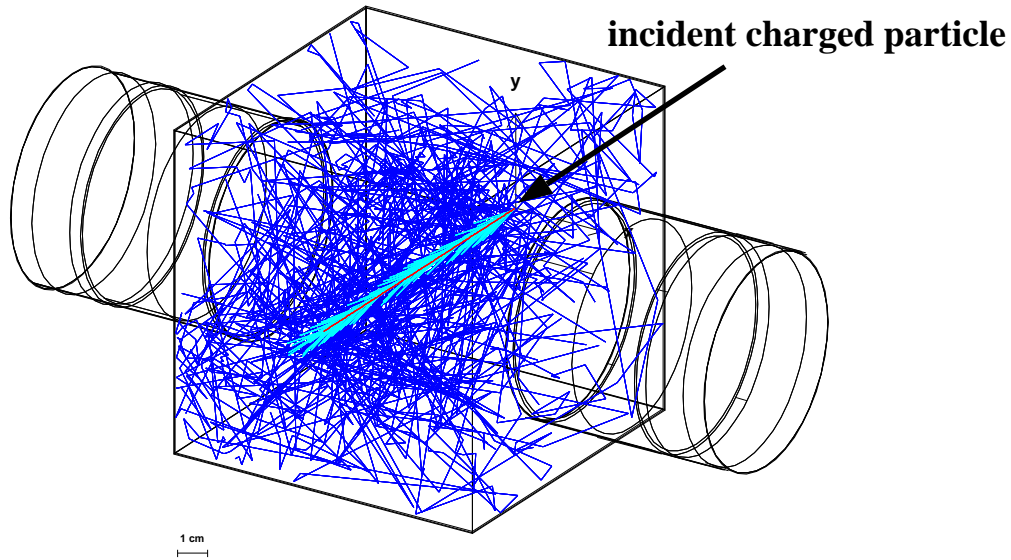


Figure 14: Event display of the Monte-Carlo simulation. The lines are the photon trajectories.

Figure 15, R.Suda et al., NIM-A

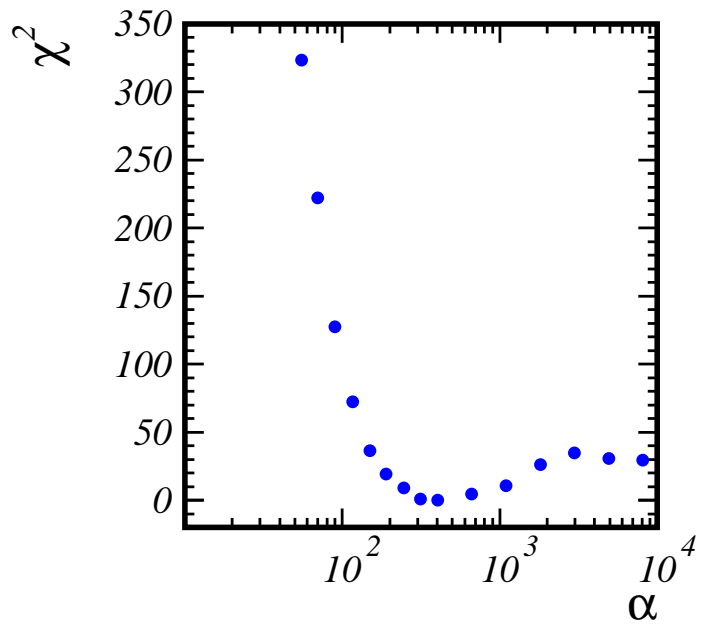


Figure 15:  $\chi^2$  versus  $\alpha$ . The details of parameter  $\alpha$  can be found in the text.

Figure 16, R.Suda et al., NIM-A

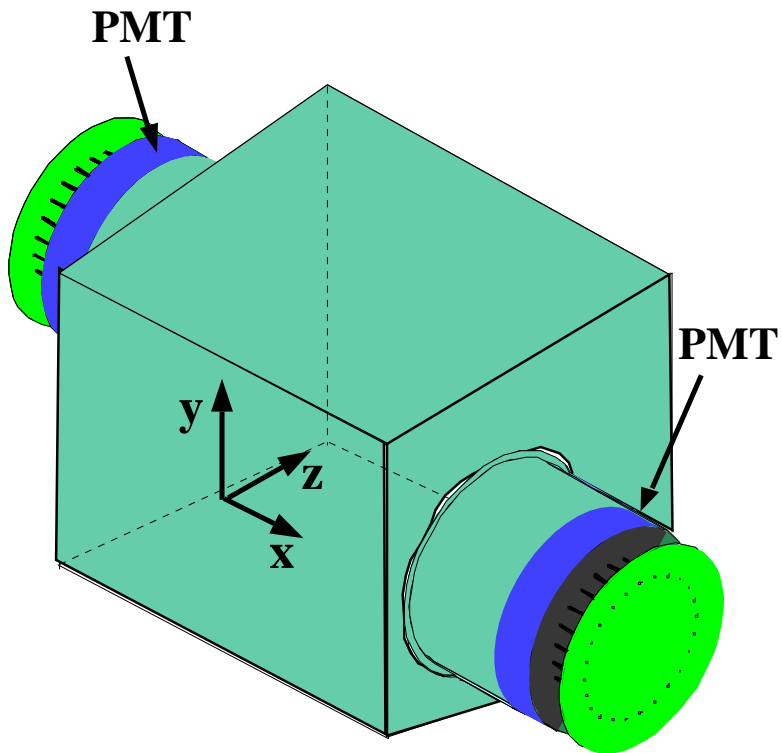


Figure 16: Definition of the incident beam position. The beam direction is parallel to the  $z$ -axis.

Figure 17, R.Suda et al., NIM-A

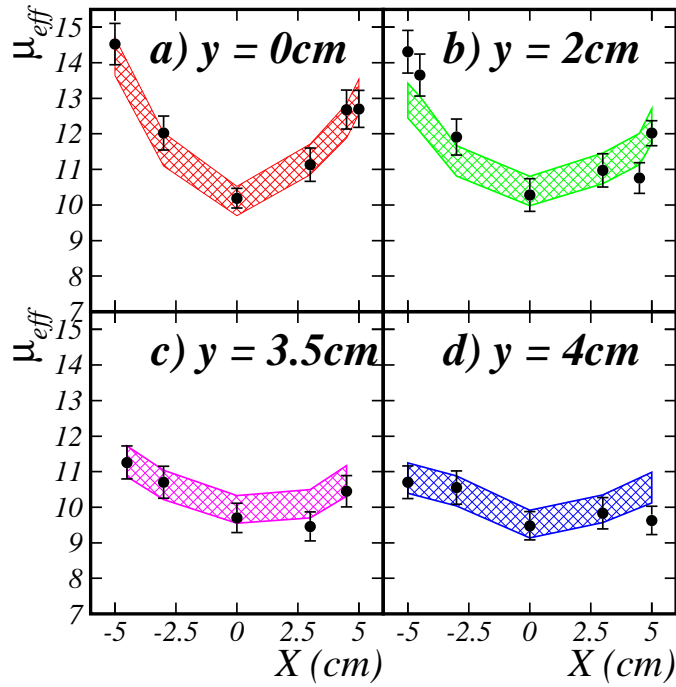


Figure 17: Position dependence of  $\mu_{eff}$  as a function of the incident beam position: (a)  $y=0$ cm, (b)  $y=2$ cm, (c)  $y=3.5$ cm, and (d)  $y=4$ cm. The points with error bars are the experimental data and the hatched areas are the Monte-Carlo predictions.

Figure 18, R.Suda et al., NIM-A

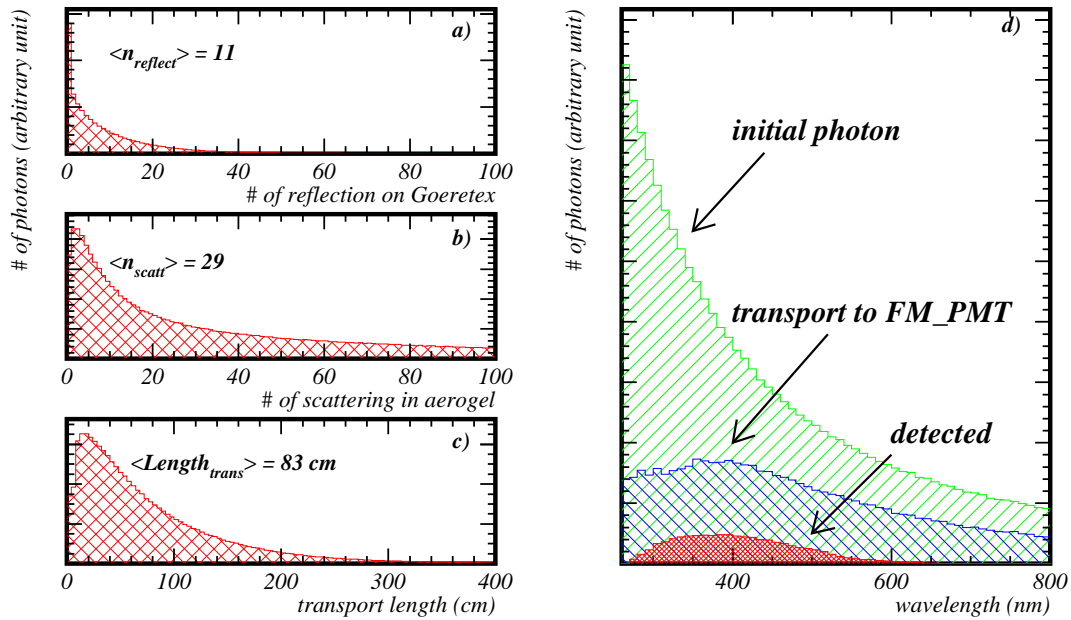


Figure 18: Various distributions predicted by the Monte-Carlo simulation: a) distribution of the number of reflections on Goretex; b) number of scatterings in aerogel; c) total transport length inside the counter box; and d) wavelength distribution of initial photon (single hatch), photon after transport to FM-PMT(cross hatch), and photon after cut of FM-PMT's quantum efficiency (dense area).

Figure 19, R.Suda et al., NIM-A

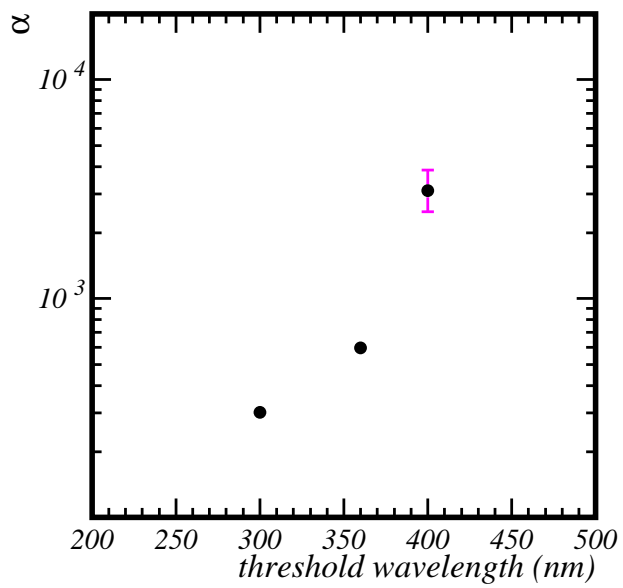


Figure 19: Evaluation of the factor  $\alpha$  using sharp-cut filters. The horizontal axis is the threshold wavelength of the filter. The vertical axis is the best  $\alpha$  values, which were obtained by comparing the Monte-Carlo simulation data with the beam data.